

1 A convection based gravity wave parameterization in
2 a general circulation model: Implementation and
3 improvements on the QBO

Sebastian Schirber¹, Elisa Manzini¹, and M. Joan Alexander²

Corresponding author: Sebastian Schirber, Max Planck Institute for Meteorology, Bundesstrasse 53, 20146 Hamburg, Germany. (sebastian.schirber@mpimet.mpg.de)

Elisa Manzini, Max Planck Institute for Meteorology, Bundesstrasse 53, 20146 Hamburg, Germany. (elisa.manzini@mpimet.mpg.de)

M. Joan Alexander, NorthWest Research Associates, CoRA Office, 3380 Mitchell Lane, Boulder, CO 80301, USA. (alexand@cora.nwra.com)

¹Max Planck Institute for Meteorology,
Hamburg, Germany.

²NorthWest Research Associates,
Colorado Research Associates Division,
Boulder, CO, USA.

4 **Abstract.** In order to simulate stratospheric phenomena such as the Quasi-
5 Biennial Oscillation (QBO), atmospheric general circulation models (GCM)
6 require parameterizations of small scale gravity waves (GW). In the trop-
7 ics the main source of GWs is convection, showing high spatial and tempo-
8 ral variability in occurrence and strength. In this study we implement in the
9 GCM ECHAM6 a source parameterization for GWs forced by convection.
10 The GW source parameterization is based on the convective heating depth,
11 convective heating rate and the background wind.

12 First, we show that the heating depth distribution of convective proper-
13 ties strongly influences the waves' source spectra. The strong sensitivity of
14 spectral wave characteristics on heating property distributions highlights the
15 importance of a realistic parameterization of convective processes in a GCM.
16 Second, with the convection based GW scheme as the unique source of GWs,
17 the GCM simulates a QBO with realistic features. While the vertical extent
18 of the easterly jet shows deficiencies, the wind speeds of the jet maxima and
19 the variance of wind alteration show a clear improvement, compared to the
20 standard model which employs a parameterization with constant, prescribed
21 GW sources. Furthermore, the seasonality of the QBO jets downward pro-
22 gression is modeled more realistically due to the seasonality of physically-
23 based gravity wave sources.

1. Introduction

24 Tropospheric waves are the key element in driving stratospheric dynamics, such as the
25 prominent Quasi-Biennial Oscillation (QBO) of equatorial zonal winds. Due to the limited
26 spatial resolution of atmospheric general circulation models (GCM), unresolved waves like
27 gravity waves (GW) need to be parameterized. Focusing on the tropics, gravity waves
28 are dominantly driven by convection, being highly variable in temporal occurrence and
29 geographical distribution. However, parameterizations of gravity wave drag force include
30 most commonly constant wave sources [*Scaife et al.*, 2000; *Giorgetta et al.*, 2002; *Shibata*
31 *and Deushi*, 2005]. In this study, we implement a gravity wave source parameterization
32 based on convection into the GCM ECHAM6, we show the dependence of the gravity
33 wave momentum fluxes on the physical input properties, and we highlight improvements
34 on the QBO amplitude and on the seasonality in the descent rate of QBO shear zones.

35 The QBO is a prominent dynamical phenomenon in the equatorial stratosphere [*Baldwin*
36 *et al.*, 2001] characterized by a quasi-periodic oscillation of zonal winds with a period of \sim
37 28 months. The QBO is driven by waves which emanate from the troposphere, propagate
38 vertically into the middle and upper atmosphere and deposit energy and momentum in
39 the region of the waves' breaking levels. The horizontal scale of the waves spans several
40 orders of magnitude, from planetary large scale Kelvin and mixed Rossby-gravity waves
41 over inertia-gravity waves down to small scale gravity waves.

42 In the modeling world, the limited spatial resolution of GCMs requires a separation into
43 resolved waves and parameterized gravity waves. Both wave components are essential in
44 order to simulate stratospheric phenomena. Several GW parameterizations include two

45 simplifying assumptions about GW source properties: (I) the source spectrum's shape of
46 excited GWs is prescribed and (II) the source spectrum is constant in space and time.
47 However observations deviate from these assumptions: (I) GWs emanate from multiple
48 sources which each show unique spectral characteristics depending on the source [*Alexan-*
49 *der et al.*, 2010]. Besides orographically based GWs, whose effects are usually represented
50 by a separate parameterization [*McFarlane*, 1987], GWs are generated by frontal sys-
51 tems, convection and more general tropospheric instabilities. (II) These sources exhibit
52 high spatial and temporal variability, implying similar variability for the excited GWs;
53 for more details on GWs see the review paper by *Fritts and Alexander* [2003]. Focus-
54 ing on the tropics, theoretical [*Salby and Garcia*, 1987], observational [*Pfister et al.*, 1993;
55 *McLandress et al.*, 2000; *Geller et al.*, 2013] and numerical studies [*Alexander and Holton*,
56 1997; *Piani et al.*, 2000; *Lane et al.*, 2001; *Song et al.*, 2003] attribute gravity wave activity
57 in the stratosphere to the underlying convection. In the tropics it is therefore reasonable
58 to assume that convection plays the dominant role in GW generation.

59 Physically based source parameterizations take account of GWs excited by convection
60 [*Chun and Baik*, 2002; *Beres et al.*, 2004]. These parameterizations generate an interactive
61 source spectrum based on the latent heating properties and the background wind. The
62 advantages of such an approach concentrate on the following aspects. First, the amount
63 of excited momentum flux shows a model-intrinsic temporal and spatial variability which,
64 second, is also prone to changes on a climatological timescale. Third, the spectral shape
65 depends on the physical properties of the modeled convective event, which removes the
66 need to subjectively prescribe the shape of the source spectrum. The last aspect is empha-
67 sized by *McLandress and Scinocca* [2005] who show that three different GW propagation

68 schemes can be tuned in a way to yield nearly identical responses on the drag profiles. The
69 authors conclude that models would benefit rather from a more realistic source spectrum
70 than from a better dissipation mechanism.

71 Several model studies implement aspects of a convection based GW source parameter-
72 izations into GCMs. Whereas *Geller et al.* [2011] add a prescribed seasonal variation in
73 space and time on the amplitude of prescribed GWs, *Richter et al.* [2010] present a con-
74 figuration of the Whole Atmosphere Community Climate Model (WACCM) with entirely
75 physically based GW source parameterizations. *Lott and Guez* [2013] simulate a QBO
76 with the GCM LMDz, introducing a stochastic GW parameterization in which the waves'
77 amplitudes are directly linked to the modeled heating rates. Concentrating on the QBO,
78 *Kim et al.* [2013] show improvements of the simulated QBO in the Met Office Unified
79 Model due to an implementation of the source parameterizations after *Chun and Baik*
80 [2002], which generates roughly 50% of the total GW fluxes in the tropics.

81 In this study we analyse effects of a convection based gravity wave scheme which repre-
82 sents the unique source of tropical GWs in an atmospheric GCM. Given this configuration
83 we are able to show the full effect of the source variability on the mean stratospheric state.
84 We further highlight the sensitivity of the GW source parameterization to the convection
85 scheme and isolate the properties which dominate the different spectral characteristics of
86 the source spectra.

2. Experimental setup

2.1. A climate model with three GW parameterizations

87 We use the atmospheric general circulation model ECHAM6 [*Stevens et al.*, 2013],
88 the latest version of the atmospheric component of the earth system model developed

89 at the Max Planck Institute for Meteorology (MPI-ESM) [*Giorgetta et al.*, 2013]. The
90 simulations performed here use a spectral truncation at wavenumber 63 and an associated
91 Gaussian grid of $\sim 1.9^\circ$ resolution. The vertical grid consists of 95 hybrid sigma pressure
92 levels, with a spacing of roughly 700m in the lower stratosphere, resolving the atmosphere
93 from the surface up to 0.01 hPa. In ECHAM6 the parameterization of cumulus convection
94 is based on the mass-flux scheme by *Tiedtke* [1989] with modification for deep convection
95 incorporated by *Nordeng* [1994]. The model parameterizes the effects of unresolved, non-
96 orographic GWs with a scheme after Hines which is based on the Doppler spread theory
97 [*Hines*, 1997a, b]. The prescribed spectrum of waves emanating from the troposphere is
98 broad band with constant amplitude in time and space, although in the standard model
99 setup, a latitudinal amplitude enhancement is introduced around the equator in order to
100 obtain a QBO with a realistic period [*Schmidt et al.*, 2013].

101 In addition to the Hines scheme, we implement the convection based GW source param-
102 eterization after *Beres et al.* [2004] which is coupled to the GW propagation parameter-
103 ization after *Alexander and Dunkerton* [1999]. Since convection is the primary source of
104 tropical GW, which are covered by the Beres scheme, we disable the Hines scheme within
105 the tropics (latitude $|\Phi| \leq 20^\circ$) entirely by setting u_{rms} , the parameter for the source
106 strength, to 0 m/s . Outside the tropics, the Hines scheme increases linearly between
107 $20^\circ \leq \Phi \leq 30^\circ$ and remains constant with u_{rms} at 1 m/s in the extratropics ($|\Phi| \geq 30^\circ$).
108 This somewhat arbitrary latitudinal partition of the two GW parameterizations is based
109 on the latitudinal extent of the Beres scheme, shown in figure 1 which is discussed in
110 more detail in section 3. The orographic GW scheme [*Lott and Miller*, 1997] is primarily
111 active in the extratropics and remains untouched in this model setup. In the chosen set-

112 ting with the non-orographic Hines and Beres GW source parameterizations, the Beres
 113 scheme produces additional wave momentum flux in the extratropical regions of the storm
 114 tracks. We decide to include this contribution for two reasons: first the additional drag
 115 does not deteriorate the model's zonal mean circulation (not shown); second an arbitrary
 116 and artificial latitudinal restriction to the tropics is not based on physical arguments.

2.2. Mechanisms of a convection based GW scheme and implementation

117 The Beres scheme produces a spectrum of gravity waves depending on the latent heating
 118 properties and the background wind in grid boxes with active convection. The param-
 119 eterization generates an individual distribution of wave momentum flux $B_0 = \overline{u'w'}$ in
 120 $[m^2/s^2]$ as a function of horizontal phase speed c_p in $[m/s]$. The shape and amplitude of
 121 the individual source spectra are dependent on the heating depth, the heating rate, the
 122 mean wind in the heating region and several prescribed parameters, each described briefly
 123 in the following paragraphs. For a more quantitative description including a theoretical
 124 derivation and detailed equations for the spectrum of source momentum flux see *Beres*
 125 *et al.* [2004].

The vertical extent of condensational heating within a cloud, the heating depth H_q , governs the dominant vertical wavelength of the excited waves. Since the vertical wavelength translates to a horizontal phase speed, the heating depth determines the position of the maxima in the phase speed spectrum: Large heating depths generate GW spectra peaking at high phase speeds, whereas small heating depths generate GW spectra peaking at low phase speeds. Being an equally important input variable, the vertical mean heating rate Q_0 strongly influences the overall amount of momentum flux, the wave's amplitude. In the employed GCM, the convection parameterization does not provide information

about individual convective events and the associated heating properties, like Q_0 , of these sub-grid scale events. The bulk mass flux scheme rather gives mean heating properties of all single convective events occurring within one gridbox. Under the assumption that the mean effect of all individual convective events is realistically represented by the bulk scheme, we estimate the heating rate in a simple approach as

$$Q_0 = \frac{Q_{max}}{C_F} \quad (1)$$

126 with Q_{max} being the peak heating rate within the GCM grid box and C_F the fraction of
 127 convection, which is assumed to be a constant 3.5% of a grid box. We highlight that the
 128 heating rate acts strongly nonlinear on the wave amplitudes: $B_0 \propto Q_0^2$, see equation (30)
 129 in *Beres et al.* [2004]. Therefore the heating rate characteristics of the convection scheme,
 130 and in particular heating rate distributions at different heating depths, are crucial for the
 131 shape of the GW source spectrum.

The horizontal wind shear across the vertical extent of the heating governs the asymmetries of the source spectra. The wind shear $\langle \frac{\partial U}{\partial z} \rangle$ is calculated as the mean background wind relative to the wind at 700hPa height via

$$\left\langle \frac{\partial U}{\partial z} \right\rangle = \int_{H_b}^{H_t} (u(h) - u_{700}) dh \quad (2)$$

132 with H_b the cloud base and H_t the cloud top, $u(h)$ the horizontal wind speed projected
 133 onto the plane of the horizontal wind at 700hPa, u_{700} , which is assumed to act as the
 134 steering level of the convective cell. Given a positive wind shear $\langle \frac{\partial U}{\partial z} \rangle$, momentum fluxes
 135 with negative phase speeds relative to u_{700} dominate the spectrum and vice versa [*Pfister*
 136 *et al.*, 1993]. The reason for this upstream enhancement of momentum fluxes is twofold.
 137 On one hand, a mechanism similar to critical level filtering reduces momentum fluxes

138 of waves propagating in the direction of the storm-relative mean wind. On the other
139 hand, a mechanism similar to the “obstacle effect“ increases momentum fluxes of waves
140 propagating in the opposite direction of the storm-relative mean wind; see *Beres et al.*
141 [2002] for a more detailed explanation. The horizontal orientation of phase speeds is
142 determined by the steering level of a convective cell, chosen as the horizontal wind at
143 $700hPa$. Analogously to the assumption in the previous paragraph about mean gridbox
144 heating, we assume that the mean gridbox values of wind are representative for wind
145 of the convective fraction of the gridbox. In the two azimuths of wave orientation, the
146 phase speeds are Doppler shifted with respect to the wind speed at $700hPa$. The source
147 spectrum spans waves from $-100m/s$ to $100m/s$ with a resolution of $1m/s$.

148 In contrast to the preceding input variables which are interactively given by the GCM
149 at each timestep, the source parameterization also requires several constant parameters
150 which need to be prescribed. Following the nomenclature from *Beres et al.* [2004], we use
151 $L = 1000km$ for the spatial averaging domain and $\sigma_x = 3.5km$ for the horizontal extent
152 of the individual convective cell. The parameterization initiates waves only when the
153 convection scheme is active and omits shallow convection by applying a minimum heating
154 depth of $2.5km$. In order to account for the earth’s sphericity, the source spectrum is
155 scaled by latitude with $B = \rho_0 \cdot B_0 \cdot \cos(\Phi)$. Waves are launched at the cloud top,
156 with ρ_0 in B the density at cloud top, from where the propagation routine by *Alexander*
157 *and Dunkerton* [1999, hereafter AD99] calculates for each individual phase speed bin its
158 corresponding breaking level in the atmosphere above. The scheme with modifications
159 after *Ortland and Alexander* [2006] is based on the simple assumption that momentum
160 fluxes carried by waves are deposited entirely at the initial onset of linear instability.

161 Given the background wind and density profiles, this concept allows a mapping of a
162 tropospheric spectrum of momentum flux to mean flow acceleration in the layers above.
163 We use a horizontal wavelength $\lambda_h = 1000km$ and an intermittency factor $\epsilon = 0.003$. For a
164 detailed explanation of the concept of intermittency see *Alexander and Dunkerton* [1999].
165 In our application with 201 discretely resolved spectral phase speed bins, $\epsilon \cdot 201 \simeq 0.6$
166 describes the occurrence of any spectral point, a value of order one.

2.3. Experiments and observational datasets

167 We explore the effects of the Beres scheme, coupled to AD99, (ECHAM6-Beres) in
168 comparison with a control run which includes a GW parameterization with constant GW
169 sources (ECHAM6-Hines). For both experimental setups we perform a 30 year atmo-
170 spheric simulation with prescribed climatological sea surface temperatures (SST) and sea
171 ice concentrations (SIC), compiled from observed SSTs and SICs. We use monthly mean
172 values of 30years as standard temporal resolution for the shown plots, but model data
173 to compile figures 2, 4 and 5 consist of 6-hourly instantaneous output covering 5 years.
174 In order to evaluate zonal winds U of the two model setups we use two different reanal-
175 ysis products, NCEP [*Kistler et al.*, 2001] and ERA-Interim [*Dee et al.*, 2011]. For the
176 EOF analysis of section 4.2.2, we use monthly mean zonal winds based on radiosonde
177 observations at three equatorial stations and compiled at Freie Universität Berlin (FUB)
178 (<http://www.geo.fu-berlin.de/en/met/ag/strat/produkte/qbo/>).

179 For the evaluation of quantities of the convection scheme in section 3.3, we derive from
180 observations two quantities: a maximum heating rate distribution and a cloud top distri-
181 bution. First, the heating rates are derived from rain rates provided by Tropical Rainfall
182 Measurement Mission (TRMM) using the algorithm [*Ryu et al.*, 2011] that includes both

183 convective and stratiform rain types. Second, cloud top heights are derived from global
184 merged infrared satellite measurements of brightness temperature using the NCEP reanal-
185 ysis to estimate height [*Ortland et al.*, 2011]. Note that the two employed observational
186 quantities are not measured directly but are rather products derived from observations.
187 Therefore, retrieval errors in the original observations and simplified assumptions in the
188 derivation of the final product introduce additional uncertainty. In order to compare
189 cloud observations with model data in a consistent way, we use temporally instantaneous
190 data every 3 hours covering the year 2007, we remove non-cloudy data points and average
191 observations spatially on $2^\circ \times 2^\circ$ resolution before performing the analysis.

3. A variable source spectrum of GW momentum flux

192 In this chapter we highlight the fundamental aspects that are introduced by a convection
193 based parameterization for gravity waves. First, we examine the temporal and spatial
194 distribution of excited momentum flux, concentrating on the overall amount of momentum
195 flux by integrating the source spectrum. In a second step, we look in more detail at
196 the spectral characteristics of the source spectrum and provide the link between resolved
197 input quantities, such as background wind and convective properties, and source spectrum
198 properties, like its shape and its asymmetry. Having identified the decisive properties of
199 the input quantities, we evaluate the quantities produced by the model with observational
200 datasets.

201 As described in section 2.2, waves are launched along the direction of u_{700} which results
202 in a meridional and zonal component in wave forcing and drag. Since the orientation of
203 u_{700} is oriented dominantly in the zonal direction, the source spectrum in the meridional
204 direction only reaches approximately 30% of the wave amplitude in zonal direction (not

shown). Because we additionally focus on the zonally oriented winds of the QBO, we
restrict the following analysis to zonal components even though waves are also launched
in the meridional direction.

3.1. Spatial distribution and seasonality of momentum flux

The GW source spectrum of momentum fluxes from the Beres scheme shows tempo-
ral and spatial variability due to the parameterization's coupling to resolved quantities.
Largest source momentum fluxes occur in tropical regions, $|\Phi| < 20^\circ$, where convection
is most active throughout the year, see figure 1(a). However the parameterization also
initiates waves in the midlatitudinal regions of the storm tracks, which are more active
in the southern hemisphere. Since cloud heating depths are bigger in the tropics than in
the midlatitudes, the wave spectrum peaks at and extends to higher phase speeds in the
tropics compared to the midlatitudes. The phase speed spectrum is Doppler shifted with
respect to the 700hPa zonal wind which is particularly important at the midlatitudes
where a nonzero background wind prevails. In the tropics however, mean background
winds are small which leads to a source spectrum with peak momentum fluxes at about
 $+20m/s$ and $-20m/s$ phase speed, see figure 1(b). The source spectrum compares well in
latitudinal distribution with results from the WACCM model with the same GW source
parameterization [Beres et al., 2005; Richter et al., 2010]. Besides differences in the con-
vection parameterization between the two model version, the implementation of the Beres
scheme in WACCM also includes a base limit for when the Doppler shift is applied: Only
when the wind speed at 700 hPa is above 10 m/s, the phase speeds of the source spectrum
are Doppler shifted. An inclusion of this base limit into our code would generate a source
spectrum with momentum fluxes dominating at positive phase speeds (not shown). How-

227 ever we remove this, somewhat arbitrary, limit on the Doppler shift in our implementation
228 of the code. Therefore, while positive phase speeds dominate the source spectrum in the
229 WACCM model, ECHAM6-Beres shows more momentum flux at negative phase speeds
230 than at positive phase speeds.

231 The source momentum flux shows a strong seasonal cycle, manifested in the mean
232 seasonal spectra and the annual cycle of integrated source momentum flux, shown in
233 figure 1 (b,c). The amount of momentum flux peaks in spring and shows a minimum in
234 late summer, which quantitatively represents a reduction of approximately 40% from the
235 peak in April to the minimum in August. The seasonality in source momentum flux is
236 the basis for further analysis on the seasonality of the QBO in section 4.2.

237 It would be desirable to be able to identify a single physical input quantity which causes
238 the seasonality in the amount of excited momentum flux B of figure 1(c). Even though
239 the seasonality of the heating rate Q_0 is dominating the seasonality of B (not shown), we
240 can't isolate a single, unique physical quantity which fully explains the seasonal cycle of B .
241 Besides the seasonality in Q_0 , variability in tropospheric wind shear and other convective
242 properties also contribute to the seasonal cycle in the amount of source momentum flux.
243 In the following two sections however, we individually highlight the two most relevant
244 physical input quantities, the background wind and the convective heating properties,
245 which decisively control the characteristics of the source spectrum.

3.2. Effect of the background wind on the source spectrum

246 We show the effect of the background wind on the source spectrum for two selected
247 regions, centered over the Indonesian archipelago and over South America. The source
248 spectra in these two regions exhibit strong asymmetries, favouring momentum fluxes with

249 positive phase speeds over Indonesia and momentum fluxes with negative phase speeds
250 over South America, see figure 2(a,c). The asymmetries are dominated by deep convective
251 clouds, depicted by the blue curve, whereas the contribution of the more shallow clouds
252 is almost symmetric, depicted by the orange curve in figure 2(a,c).

253 As outlined in section 2, a positive wind shear produces a source spectrum with domi-
254 nating negative phase speeds and vice versa. This result from a case study with a cloud
255 resolving model [*Beres et al.*, 2002] and localised observations [*Pfister et al.*, 1993] is now
256 extended to large geographical regions by model data of GWs generated with linear the-
257 ory [*Beres et al.*, 2004]. The histogram of wind shear $\langle \frac{\partial U}{\partial z} \rangle$ in figure 2(b,d) shows a clear
258 non-zero mean value, especially for the regime of deep convective clouds which cause the
259 spectral asymmetry. While a negative wind shear leads to a source spectrum with dom-
260 inant positive phase speeds over Indonesia, a positive wind shear can be associated with
261 a source spectrum with dominant negative phase speeds over South America.

262 The modeled wind shear over the two selected regions agrees with reanalysis data, see
263 figure 3. While ECHAM shows a westerly bias in the upper troposphere in both regions,
264 the vertical wind shear in the model is qualitatively consistent with reanalysis. In the
265 free atmosphere, the region centered over the Indonesian archipelago shows a negative
266 wind shear and the region over South America a positive wind shear. To summarize
267 this subsection, different background winds, which qualitatively agree with reanalysis
268 products, cause significant asymmetries in the GW source spectrum in large geographical
269 regions.

3.3. Effect of convective heating properties on the source spectrum

270 The source momentum fluxes show a strong dependence on properties of the convection
271 scheme. The most important quantities are the heating depth and the maximum heating
272 rate within a GCM grid box, with a particular importance on the histogram of heating
273 depth and the heating rate's dependence on heating depth. The emitted source momentum
274 flux is separated into the two regimes of shallow (orange) and deep (blue) convective
275 clouds, see figure 4, illustrated by the peak at higher phasespeeds for deep convective
276 clouds. The total spectrum (black) results from a superposition of both heating depth
277 regimes. The separation into two heating depth regimes can be observed in more detail in
278 figure 5(a) which shows the amount of excited momentum flux B as a function of heating
279 depth. Shallow clouds with 2.5 km and 5 km heating depth and deep convective clouds
280 with around 15 km heating depth contribute significantly to the entire source spectrum.
281 Convective clouds with heating depths in the range 6 – 12 km however produce very little
282 momentum flux.

283 The momentum flux histogram in figure 5(a) corresponds only partly to the heating
284 depth histogram in figure 5(b), which shows that the convection scheme produces most
285 frequently rather shallow clouds ($< 6km$), very few midlevel clouds ($6 - 12km$) and
286 some deep convective clouds ($> 12km$). The two histograms do not agree because the
287 amplitude of the source spectrum is additionally scaled by a factor $\propto Q_{max}^2$ which strongly
288 increases with increasing heating depth, see 5(c). This nonlinear amplification of the
289 source spectra's amplitudes leads to a peak in B at large heating depth, even though
290 convection with large heating depth does not occur very frequently.

291 A comparison with TRMM and satellite based observations reveals deficiencies in the
292 convection scheme, most apparent in the histogram of heating depth, see figure 5(b).

293 Observations show a continuous distribution with dominating midlevel convection which
294 peaks at 9 km and ends at 12km heating depth rather than the double peak distribution
295 that the convection scheme produces. Most obvious discrepancy appears in the range of
296 6 – 12km heating depth, where the model lacks convection, and at large heating depths,
297 where the model produces convection in contrast to the observations. For a more detailed
298 discussion and consequences due to the difference in observations and model data see
299 chapter 5. The model’s distribution of heating rate Q_{max} however compares qualitatively
300 to the observations, see figure 5(c), with a strong increase in Q_{max} with increasing heating
301 depth. The kinks at the upper end of the distributions should not be over-interpreted
302 since these are prone to sampling errors due to the very small number of events at the
303 upper end of the heating depth distribution.

4. The QBO

304 ECHAM6-Beres produces a QBO with realistic features, see figure 6. The simulated
305 evolution of zonal winds shows prominent features of the QBO: A periodic alternation of
306 westerly and easterly winds, an asymmetry in amplitude with easterly jets being stronger
307 than westerly jets, and a mean period of ~ 27.5 months. The simulated period is tuned
308 with the parameters C_F and L , see section 2 for a more detailed parameter description
309 and section 5 for a more thorough discussion on parameter tuning.

4.1. Comparison with ECHAM6-Hines and ERA-Interim

310 A comparison with the QBO of ECHAM6-Hines and of ERA-Interim shows improve-
311 ments and deficiencies of the QBO simulated with ECHAM6-Beres. Both ECHAM6-Hines
312 and ECHAM6-Beres produce a QBO with too strong westerly jet maxima, figure 7. How-

313 ever this bias is strongly reduced in ECHAM6-Beres. Also the bias in the easterly jet
314 maxima of ECHAM6-Hines is reduced such that the wind speed maximum in ECHAM6-
315 Beres agrees with reanalysis. The easterly jet in ECHAM6-Beres does not extend as far
316 downwards as in reanalysis data, but ends at 50 hPa rather than 90 hPa as in the reanal-
317 ysis, which could partly be a result of the generally weaker easterly jet in ECHAM6-Beres.
318 The westerly jet extends towards $\sim 75 hPa$ in both model simulations and agrees well
319 with ERA-Interim. In both model simulations, the QBO extends too far into the upper
320 stratosphere above 10 hPa , with an improvement in ECHAM6-Beres. However this im-
321 provement comes at the cost of pronounced easterlies at about 1 hPa in ECHAM6-Beres.

322 The zonal wind variances in ECHAM6-Beres agree well with reanalysis, see figure 8.
323 The wind variance in QBO-related periods agrees not only in amplitude but also in the
324 position of the peak, a clear improvement over ECHAM6-Hines. The wind variance at
325 1 hPa in ECHAM6-Beres agrees reasonably well with ERA-Interim. At higher altitudes
326 around 0.1 hPa , ECHAM6-Beres simulates the decrease in wind variance more realistically
327 than ECHAM6-Hines, but shows higher values than the reanalysis.

328 The improvement in QBO wind variance in ECHAM6-Beres can partly be explained by
329 different drag profiles in ECHAM6-Beres and ECHAM6-Hines. Figure 9 compares drag
330 profiles from simulations performed over one month and initiated with the same back-
331 ground state. The short temporal coverage guarantees that both parameterizations react
332 to a nearly identical background wind profile. Following *Scaife et al.* [2000], lowering the
333 waves' breaking levels reduces primarily the QBO amplitude. The comparison between
334 both parameterizations shows that the peaks in the drag profile in ECHAM6-Beres are sit-

335 uated at lower altitude than in ECHAM-Hines, thus leading to a reduced QBO amplitude
 336 and QBO wind variance.

4.2. Seasonal effects of parameterized, variable GW sources on the QBO

337 Due to the physically based GW sources, figure 1(c) shows a strong seasonal cycle in
 338 the amount of wave momentum flux emanating from the troposphere. We establish a
 339 link between the seasonality of GW source strength, the seasonality in the amount of
 340 drag in the lower stratosphere, and finally the seasonality of QBO phase progression rate.
 341 Following the analysis by *Wallace et al.* [1993], who apply an EOF analysis on the zonal
 342 winds, we further extend the concept in order to show the seasonality of individual drag
 343 components and of the total drag.

4.2.1. Construction of an EOF analysis

We apply an EOF analysis on a monthly (t) based timeseries of meridionally averaged
 (5°N to 5°S lat) zonal mean anomalies of a variable $\chi'(z, t)$, computed on each vertical
 level z between 10 and 70 hPa . The analysed quantities χ' are zonal wind U , total drag
 on the zonal wind $\frac{\partial U}{\partial t}|_{GWD+\nabla \cdot EP+ADV}$ and the individual drag components due to gravity
 waves $\frac{\partial U}{\partial t}|_{GWD}$, due to the divergence of the Eliassen-Palm flux of resolved waves, $\frac{\partial U}{\partial t}|_{\nabla \cdot EP}$,
 and due to horizontal and vertical advection $\frac{\partial U}{\partial t}|_{ADV}$. All data is smoothed by a simple
 3-months running average, but in contrast to *Wallace et al.* [1993] and *Taguchi* [2010] not
 deseasonalized. Each quantity χ' can be expressed as a linear combination of empirical
 orthogonal functions *EOF*, which are dependent on height but constant in time, and
 principal components *pc* which represent the corresponding timeseries:

$$\chi'(z, t) \simeq EOF_1(z) \cdot pc_1(t) + EOF_2(z) \cdot pc_2(t) \quad (3)$$

345 omitting higher orders since the first two *EOFs* cover most of the variance; in the case of
 346 U , the two leading *EOFs* account for 96.1% of the total variance, see figure 10(a). The
 347 *EOFs* of the drag components due to GW and the total drag are shown in figure 10(b)
 348 and (c).

Due to the high amount of covered variance by the two leading *EOFs*, the 2-dimensional phase space of the *pcs* serves as a good proxy for the temporal evolution of the QBO, displayed in 10(d-f). Each point $\psi(t)$ in phase space corresponds to a state of the QBO in a certain month, while in the course of a full QBO cycle, the points form a circle in phase space. Given the circular characteristics of the temporal evolution in phase space, the data points ψ can be represented by polar coordinates with the radial coordinate $|\psi|$

$$|\psi(t)| = \sqrt{pc_1(t)^2 + pc_2(t)^2} \quad (4)$$

and angular coordinate ϕ

$$\phi(t) = \text{atan2}(pc_1(t), pc_2(t)) \quad (5)$$

349 with the function *atan2* being based on the function *arctan*, but extended to return the
 350 appropriate quadrant of the computed angle. The function *atan2* returns a value in $[0, 2\pi[$
 351 which correspond to angles of the entire circle.

In the case of U , we estimate the progression rate of the QBO phase ϕ'_U in month t as the rate of change of the angle ϕ ,

$$\phi'_U(t) = \frac{1}{2 \cdot 2\pi} [\phi(t-1) + \phi(t+1)] \quad (6)$$

352 with the units *cycle/month*. In the cases when the EOF analysis was applied to the
 353 different drag components, we use $|\psi(t)|$ as a proxy for the amount of drag in the particular
 354 month. For each month we calculate ϕ' from the phase space in U and $|\psi|$ for the individual

355 drag components and compile the data to show the seasonality of the computed quantities,
 356 displayed in figure 11.

357 4.2.2. Results on the seasonal timescale

358 The seasonality of QBO phase progression and the seasonality of the total drag are
 359 in good agreement, peaking in May and showing a second local maximum in Octo-
 360 ber/November, shown for both ECHAM6-Beres in figure 11 (a) and ECHAM6-Hines in
 361 figure 11 (c). This objective statistical analysis confirms the physical understanding that
 362 the QBO descends faster in times when more drag is exerted. Focusing on the individual
 363 drag components in figure 11 (b) and (d), we see that each component exhibits different
 364 characteristics in seasonality. While $\frac{\partial U}{\partial t}|_{\nabla \cdot EP}$ shows a semiannual oscillatory behavior with
 365 peaks in March and October, $\frac{\partial U}{\partial t}|_{ADV}$ has a minimum in late spring and maximum in late
 366 summer which opposes the maxima and minima of the entire drag of figure 11 (a,c). Both
 367 $\frac{\partial U}{\partial t}|_{ADV}$ and $\frac{\partial U}{\partial t}|_{\nabla \cdot EP}$ show a qualitatively similar behaviour in both model versions. The
 368 seasonality of the drag due to GW however differs for the different GW parameteriza-
 369 tions. While both $\frac{\partial U}{\partial t}|_{GWD}$ in ECHAM6-Hines and $\frac{\partial U}{\partial t}|_{GWD}$ in ECHAM6-Beres show an
 370 annual variation with maximum in April/May and minimum in August/September, the
 371 seasonality in ECHAM6-Beres is more pronounced which is manifested in the stronger
 372 amplitude of the seasonal variation of $\frac{\partial U}{\partial t}|_{GWD}$.

373 Note that the entire drag in the upper panel of figure 11 is not attained by simply adding
 374 the three drag components in the lower panel. Each curve is the result of an individual
 375 EOF analysis and in the case of the total drag, the individual drag components are added
 376 before the EOF analysis is performed.

377 In figure 12, the comparison of the two model configurations with observations sug-
378 gests an improvement due to the variable GW scheme in ECHAM6-Beres. Both model
379 versions show qualitatively a consistent agreement with observations, which is caused by
380 the similar seasonality of $\frac{\partial U}{\partial t}|_{ADV}$. However adding the seasonal cycle of $\frac{\partial U}{\partial t}|_{GWD}$ in the
381 case of ECHAM6-Beres leads to better agreement with the observed seasonality. Note
382 that the mean phase progression in both ECHAM6-Hines and ECHAM6-Beres lie within
383 the 2σ ranges of the reanalysis product and that the shown improvement in QBO phase
384 progression rate in ECHAM6-Beres is statistically not significant.

5. Discussion and implications for tuning the GW schemes

385 Most parameterizations include parameters, whose values are only loosely determined by
386 theoretical arguments or observational studies but which substantially impact the output
387 of the parameterization. Changing the value of these parameters within the theoretical
388 and observational limits, in order to generate a more realistic representation of the param-
389 eterized processes or affected phenomena, remains a necessary step while implementing
390 a parameterization into a model. Here we refer to this process as 'tuning' and to the
391 adjustable parameters as 'tuning parameters'. In this study, we tune the GW source
392 and GW propagation parameterization in order to obtain a QBO; we specifically choose
393 the QBO period as the most important target criterion. In this section we focus on two
394 aspects of the source spectrum, the spectral shape and the amplitude, and we evaluate
395 potentials for tuning each of the two aspects in the context of the Beres + AD99 setup.

5.1. Spectral characteristics of the source momentum fluxes: Tuning the propagation scheme

396 The comparison of convection properties of ECHAM6-Beres with observational products
397 reveals discrepancies which affect the source spectrum’s shape. The overrepresentation
398 of deep convective clouds in ECHAM6, figure 5(b), results in large source momentum
399 fluxes at large heating depths, see the peak at 15 *km* in figure 5(a). This bias at deep
400 convective events leads to an overrepresentation of source momentum fluxes at high phase
401 speeds (figure 4). Additionally, the design of the Beres scheme already entails an un-
402 derrepresentation of source momentum flux at low phase speeds: The parameterization
403 does not include the waves generated by the obstacle effect, or “moving mountain mecha-
404 nism” [Lane *et al.*, 2001]. These waves are similar to orographic GW such that the waves
405 are stationary with respect to the convective cell, thus producing momentum fluxes at
406 low phase speeds. For a more detailed discussion on the difficulties of implementing the
407 obstacle effect into GW source parameterizations see Alexander *et al.* [2006]. The com-
408 bined effect of both aspects, the bias in the convection scheme and the missing obstacle
409 effect, suggests an underrepresentation of small phase speed waves, $|c_p| < 15$ *m/s*, and
410 an overrepresentation of large phase speed waves, $|c_p| > 40$ *m/s*, in the modeled source
411 spectrum.

412 Results from other model studies and observations support the existence of a modeled
413 overrepresentation of large phase speed waves and underrepresentation of small phase
414 speed waves. Several case studies performed with cloud resolving models show source
415 spectra which peak in the range between 5 and 20 *m/s* [Alexander and Holton, 1997;
416 Piani and Durran, 2001; Alexander *et al.*, 2006; Kuester *et al.*, 2008]. The observational

417 study based on localized airborne measurements by *Pfister et al.* [1993] reveals source
418 spectra peaking between 0 and 10 m/s , depending on the background wind. *Jewtoukoff*
419 *et al.* [2013] analyse high frequency balloon measurements in the stratosphere which show
420 GW spectra peaking between 0 and 15 m/s , while corresponding numerical simulations
421 show peaks at higher phase speeds. Even though one referenced spectrum peaks at 20
422 m/s , which is in accordance to the peak of the modeled source spectrum (figure 1), none
423 of the referenced spectra shows such pronounced momentum fluxes at phase speeds bigger
424 than 40 m/s .

425 The Beres scheme provides very limited possibilities for tuning the spectral shape be-
426 cause the spectral characteristics are dependent on the convective properties and the
427 background wind, a fundamental concept of the parameterization. If these physical in-
428 put values however exhibit a robust bias, only a rather brute-force manipulation of the
429 spectral shape is possible, e. g. restricting momentum fluxes to phase speeds $< 50 m/s$.
430 Even though other studies and observations suggest that the modeled source spectrum
431 shows deficiencies, we refrain from manually changing the source spectrum for two reasons:
432 First, the high degree of unphysical subjectiveness that would be incorporated into the
433 parameterization and second, the lack of sufficient comprehensive observations of global
434 source spectra characteristics.

435 However, the indicated underrepresentation of momentum fluxes at low phase speeds is
436 reflected in the values chosen for parameters ϵ and λ_h , relevant for tuning the propagation
437 parameterization. A small value of ϵ and a large value for λ_h both decrease the levels where
438 the waves become convectively unstable, the breaking level. When tuning the propagation
439 parameterization, the values for ϵ and λ_h are chosen such that the peaks in the drag profile

440 correspond to the levels of the strongest wind shear. Given the underrepresentation of
 441 waves with low phase speeds, a high value for λ_h and a small value for ϵ are necessary
 442 that waves with large phase speeds break at much lower levels than their critical levels.

5.2. Amplitude of the source spectrum: Tuning for the QBO period

443 The range of total momentum flux excited in the tropics is well observed. Studies based
 444 on observations and cloud resolving models show mean momentum fluxes in the range
 445 $1 - 5mPa$ [*Sato and Dunkerton, 1997; Piani et al., 2000; Grimsdell et al., 2010; Geller*
 446 *et al., 2013*], while *Dunkerton [1997]* states that it requires time averaged, zonal mean flux
 447 of tropical gravity waves of approximately $1mPa$ to drive the QBO. The observational
 448 data constrain the range of total excited momentum flux for justifiable limits on tuning
 449 parameters. The two parameters C_F and L , the fraction of convection within a GCM
 450 gridbox and the spatial averaging length, respectively, influence the overall amplitude of
 451 the source spectrum. The amplitude of the source spectrum affects the amount of exerted
 452 drag on the jets of the QBO and consequently strongly determines the QBO period, see
 453 also *Scaipe et al. [2000]*. Both tuning parameters equally change the amount of momentum
 454 flux at all phase speeds of the spectrum but have no effect on the spectral shape or the
 455 temporal and spatial variability. The GW source parameterization produces, on an annual
 456 average, a mean momentum flux of approximately $3 - 3.5mPa$, see figure 1 (c). Given
 457 that the modeled amount of excited wave momentum flux compares well to observations
 458 and that with $C_F = 3.5\%$ and $L = 1000km$ the parameter values lie within a physical
 459 range, we can say that the tuning of the source parameterization obeys the limits of the
 460 observations. The tuned amplitude of the source spectrum generates a QBO period of \sim
 461 27.5 months.

6. Summary and Conclusion

462 We couple the convection based source parameterization of gravity waves (GW) af-
463 ter *Beres et al.* [2004] to the propagation parameterization after *Alexander and Dunker-*
464 *ton* [1999] and implement the schemes into the atmospheric general circulation model
465 ECHAM6. Compared to a GW source parameterization with constant, prescribed sources,
466 the Beres parameterization improves the representation of GWs in two main aspects.
467 First, the excited gravity waves show a strong spatial, figure 1(a), and temporal, figure
468 1(b,c), variability in the amount of total momentum flux. This variability is directly linked
469 to the occurrence of areas of intense convection. Second, the spectral shape characteris-
470 tics of the source spectrum is not prescribed but coupled to heating characteristics of the
471 convection scheme and the background wind. In detail, regionally different background
472 winds over South America and the Indonesian archipelago result in different shapes of
473 the source spectra, with dominating easterly and westerly waves, respectively (figure 2).
474 The analysis further reveals that the regime of deep convective clouds causes in large part
475 the spectral asymmetry, because vertical wind shears more effectively affect deep clouds
476 than shallow clouds. Studies [*Pfister et al.*, 1993] on localised geographical regions have
477 shown that wind shear causes asymmetries in the waves' source spectrum. Moreover our
478 model results also show that this effect remains important even when averaging over large
479 geographical domains covering > 10.000 km (order of 100° longitude at the equator). The
480 existence of asymmetric source spectra over large geographical regions has implications for
481 GW source parameterizations with a prescribed source spectrum. Analogously to *Geller*
482 *et al.* [2011] who prescribe a temporally varying source spectrum in amplitude, the next
483 step would be to include spatially varying asymmetric source spectra.

484 To the authors knowledge, this is the first time that an atmospheric GCM produces a
485 realistic QBO with a convection based GW source parameterization as the only source
486 of GWs, see figure 6. Compared to the previously employed GW parameterization in
487 ECHAM6, which prescribes spatially and temporally constant sources, the QBO simulated
488 with ECHAM6-Beres shows, on one hand, a slight deterioration of the vertical extent of
489 the easterly jet, shown in figure 7. On the other hand however, the wind speeds of the
490 jet maxima and the variance of wind alteration show a clear improvement, see figure 8.
491 More generally, we'd like to point out that deficiencies in QBO characteristics are not
492 necessarily linked to shortcomings in GW parameterizations. Possible deficiencies in the
493 modeled resolved waves or the upwelling will deteriorate the representation of the QBO.

494 Furthermore, we apply an EOF analysis on the QBO zonal winds and on the individual
495 drag components of the momentum budget of the QBO. The analysis shows that the
496 seasonality of the GW drag dominates the seasonality of the downward propagation of
497 the QBO jets. Note that $\frac{\partial U}{\partial t}|_{GWD}$ in figure 11(b) matches the seasonal variation in excited
498 amount of momentum flux in 1(c). Due to a more realistic, seasonally varying excitation
499 of parameterized wave fluxes from convection, the modeled QBO suggests an improvement
500 in its jet downward propagation rate, see figure 12. We point out that the EOF analysis
501 suffers several simplifications: first, the EOF analysis produces only vertically integrated
502 values of QBO related quantities, second the series of *EOFs* is truncated after the first
503 two *EOFs*, and third using the length of the vector in phase space as a proxy for the
504 amount of drag is a crude approximation. However in contrast to the given shortcomings
505 of the analysis, the strong agreement between the amount of drag and the QBO phase

506 progression in both model versions confirms the applicability of the chosen method, figure
507 11(a,c).

508 When tuning the parameterization it turns out that the amplitude of the source spec-
509 trum, which translates to the total amount of excited momentum flux, and the breaking
510 levels of the propagation parameterization are important factors to produce a QBO in
511 the chosen model setup. Within the range of physically justified limits, both the ampli-
512 tude and the breaking levels require tuning. However the shape, the asymmetries, the
513 temporal, and the spatial variability of the spectrum remain entirely based on physical
514 values, provided by the model. We showed that the physically based character of the
515 source parameterization, coupled to the propagation parameterization of AD99, improves
516 the modeled QBO.

517 **Acknowledgments.** We thank the Max Planck Society, the International Max Planck
518 Research School for Earth System Modeling and the Northwest Research Associates
519 (NWRA-CORA). Support for Joan M. Alexander was provided by grants from the US
520 National Science Foundations Physical and Dynamic Meteorology and Climate and Large-
521 scale Dynamics Programs, ATM-943506 and AGS-1318932. Simulations were carried out
522 on the supercomputing facilities of the German Climate Computation Centre (DKRZ) in
523 Hamburg. Marco Giorgetta and Thomas Krismer provided valuable feedback on earlier
524 drafts of this work. The original code for the Beres parameterization was provided and
525 adopted from WACCM.

References

- 526 Alexander, M., and J. Holton (1997), A model study of zonal forcing in the equatorial
527 stratosphere by convectively induced gravity waves, *Journal of the atmospheric sciences*,
528 *54*, 408–419.
- 529 Alexander, M. J., and T. J. Dunkerton (1999), A spectral parameterization of mean-flow
530 forcing due to breaking gravity waves, *Journal of the Atmospheric Sciences*, *56*(24),
531 4167–4182, doi:10.1175/1520-0469(1999)056<4167:ASPOMF>2.0.CO;2.
- 532 Alexander, M. J., J. H. Richter, and B. R. Sutherland (2006), Generation and Trapping
533 of Gravity Waves from Convection with Comparison to Parameterization, *Journal of*
534 *the Atmospheric Sciences*, *63*(11), 2963–2977, doi:10.1175/JAS3792.1.
- 535 Alexander, M. J., M. Geller, C. McLandress, S. Polavarapu, P. Preusse, F. Sassi, K. Sato,
536 S. Eckermann, M. Ern, A. Hertzog, Y. Kawatani, M. Pulido, T. a. Shaw, M. Sigmund,
537 R. Vincent, and S. Watanabe (2010), Recent developments in gravity-wave effects in
538 climate models and the global distribution of gravity-wave momentum flux from obser-
539 vations and models, *Quarterly Journal of the Royal Meteorological Society*, *136*(July),
540 1103–1124, doi:10.1002/qj.637.
- 541 Baldwin, M. P., L. J. Gray, T. J. Dunkerton, K. Hamilton, P. H. Haynes, W. J. Randel,
542 J. R. Holton, M. J. Alexander, I. Hirota, T. Horinouchi, D. B. A. Jones, J. S. Kinners-
543 ley, C. Marquardt, K. Sato, and M. Takahashi (2001), The Quasi-Biennial Oscillation,
544 *Reviews of Geophysics*, *39*(2), 179–229.
- 545 Beres, J., M. J. Alexander, and J. R. Holton (2002), Effects of tropospheric wind shear
546 on the spectrum of convectively generated gravity waves, *Journal of the atmospheric*
547 *sciences*, *59*(1998), 1805–1824.

- 548 Beres, J. H., M. J. Alexander, and J. R. Holton (2004), A Method of Specifying the Grav-
549 ity Wave Spectrum above Convection Based on Latent Heating Properties and Back-
550 ground Wind, *Journal of the Atmospheric Sciences*, *61*(3), 324–337, doi:10.1175/1520-
551 0469(2004)061;0324:AMOSTG;2.0.CO;2.
- 552 Beres, J. H., R. R. Garcia, B. a. Boville, and F. Sassi (2005), Implementation of a gravity
553 wave source spectrum parameterization dependent on the properties of convection in
554 the Whole Atmosphere Community Climate Model (WACCM), *Journal of Geophysical*
555 *Research*, *110*(D10), 1–13, doi:10.1029/2004JD005504.
- 556 Chun, H.-Y., and J.-J. Baik (2002), An Updated Parameterization of Convectively Forced
557 Gravity Wave Drag for Use in Large-Scale Models, *Journal of the Atmospheric Sciences*,
558 *59*(5), 1006–1017, doi:10.1175/1520-0469(2002)059;1006:AUPOCF;2.0.CO;2.
- 559 Dee, D. P., S. M. Uppala, a. J. Simmons, P. Berrisford, P. Poli, S. Kobayashi, U. Andrae,
560 M. a. Balmaseda, G. Balsamo, P. Bauer, P. Bechtold, a. C. M. Beljaars, L. van de Berg,
561 J. Bidlot, N. Bormann, C. Delsol, R. Dragani, M. Fuentes, a. J. Geer, L. Haimberger,
562 S. B. Healy, H. Hersbach, E. V. Hólm, L. Isaksen, P. Kå llberg, M. Köhler, M. Ma-
563 tricardi, a. P. McNally, B. M. Monge-Sanz, J.-J. Morcrette, B.-K. Park, C. Peubey,
564 P. de Rosnay, C. Tavolato, J.-N. Thépaut, and F. Vitart (2011), The ERA-Interim
565 reanalysis: configuration and performance of the data assimilation system, *Quarterly*
566 *Journal of the Royal Meteorological Society*, *137*(656), 553–597, doi:10.1002/qj.828.
- 567 Dunkerton, T. J. (1997), The role of gravity waves in the quasi-biennial oscillation, *Journal*
568 *of Geophysical Research*, *102*(D22), 26,053–26,076.
- 569 Fritts, D. C., and M. Alexander (2003), Gravity wave dynamics and effects in the middle
570 atmosphere, *Reviews of Geophysics*, *41*(1), 1–64, doi:10.1029/2001RG000106.

- 571 Geller, M. a., T. Zhou, R. Ruedy, I. Aleinov, L. Nazarenko, N. L. Tausnev, S. Sun,
572 M. Kelley, and Y. Cheng (2011), New Gravity Wave Treatments for GISS Climate
573 Models, *Journal of Climate*, *24*(15), 3989–4002, doi:10.1175/2011JCLI4013.1.
- 574 Geller, M. a., M. J. Alexander, P. T. Love, J. Bacmeister, M. Ern, A. Hertzog, E. Manzini,
575 P. Preusse, K. Sato, A. a. Scaife, and T. Zhou (2013), A Comparison Between Gravity
576 Wave Momentum Fluxes in Observations and Climate Models, *Journal of Climate*,
577 *26*(17), 6383–6405, doi:10.1175/JCLI-D-12-00545.1.
- 578 Giorgetta, M. A., E. Manzini, and E. Roeckner (2002), Forcing of the quasi-biennial
579 oscillation from a broad spectrum of atmospheric waves, *Geophysical Research Letters*,
580 *29*(8), 8–11, doi:10.1029/2002GL014756.
- 581 Giorgetta, M. a., J. Jungclaus, C. H. Reick, S. Legutke, J. Bader, M. Böttinger,
582 V. Brovkin, T. Crueger, M. Esch, K. Fieg, K. Glushak, V. Gayler, H. Haak, H.-D.
583 Hollweg, T. Ilyina, S. Kinne, L. Kornblueh, D. Matei, T. Mauritsen, U. Mikolajew-
584 icz, W. Mueller, D. Notz, F. Pithan, T. Raddatz, S. Rast, R. Redler, E. Roeckner,
585 H. Schmidt, R. Schnur, J. Segschneider, K. D. Six, M. Stockhause, C. Timmreck,
586 J. Wegner, H. Widmann, K.-H. Wieners, M. Claussen, J. Marotzke, and B. Stevens
587 (2013), Climate and carbon cycle changes from 1850 to 2100 in MPI-ESM simulations
588 for the coupled model intercomparison project phase 5, *Journal of Advances in Modeling*
589 *Earth Systems*, pp. n/a–n/a, doi:10.1002/jame.20038.
- 590 Grimsdell, A. W., M. J. Alexander, P. T. May, and L. Hoffmann (2010), Model Study
591 of Waves Generated by Convection with Direct Validation via Satellite, *Journal of the*
592 *Atmospheric Sciences*, *67*(5), 1617–1631, doi:10.1175/2009JAS3197.1.

- 593 Hines, C. (1997a), Doppler-spread parameterization of gravity-wave momentum deposi-
594 tion in the middle atmosphere. Part 1: Basic formulation, *Journal of Atmosphere and*
595 *Solar-Terrestrial Physics*, 59(4), 371–386.
- 596 Hines, C. (1997b), Doppler-spread parameterization of gravity-wave momentum deposi-
597 tion in the middle atmosphere. Part 2: Broad and quasi monochromatic spectra , and
598 implementation, *Journal of Atmosphere and Solar-Terrestrial Physics*, 59(4), 387–400.
- 599 Jewtoukoff, V., R. Plougonven, and A. Hertzog (2013), Gravity waves generated by deep
600 tropical convection: estimates from balloon observations and mesoscale simulations,
601 *Journal of Geophysical Research: Atmospheres*, pp. n/a–n/a, doi:10.1002/jgrd.50781.
- 602 Kim, Y.-H., a. C. Bushell, D. R. Jackson, and H.-Y. Chun (2013), Impacts of introducing
603 a convective gravity-wave parameterization upon the QBO in the Met Office Unified
604 Model, *Geophysical Research Letters*, 40(9), 1873–1877, doi:10.1002/grl.50353.
- 605 Kistler, R., W. Collins, S. Saha, G. White, J. Woollen, E. Kalnay, M. Chelliah,
606 W. Ebisuzaki, M. Kanamitsu, V. Kousky, H. van den Dool, R. Jenne, and M. Fiorino
607 (2001), The NCEPNCAR 50Year Reanalysis: Monthly Means CDROM and Documen-
608 tation, *Bulletin of the American Meteorological Society*, 82(2), 247–267.
- 609 Kuester, M. a., M. J. Alexander, and E. a. Ray (2008), A Model Study of Gravity Waves
610 over Hurricane Humberto (2001), *Journal of the Atmospheric Sciences*, 65(10), 3231–
611 3246, doi:10.1175/2008JAS2372.1.
- 612 Lane, T., M. Reeder, and T. Clark (2001), Numerical modeling of gravity wave generation
613 by deep tropical convection, *Journal of the atmospheric sciences*, 58, 1249–1274.
- 614 Lott, F., and L. Guez (2013), A stochastic parameterization of the gravity waves due
615 to convection and its impact on the equatorial stratosphere, *Journal of Geophysical*

- 616 *Research: Atmospheres*, pp. n/a–n/a, doi:10.1002/jgrd.50705.
- 617 Lott, F., and M. Miller (1997), A new subgridscale orographic drag parametrization: Its
618 formulation and testing, *Quarterly Journal of the Royal Meteorological Society*, *123*,
619 101–127.
- 620 McFarlane, N. (1987), The effect of orographically excited gravity wave drag on the gen-
621 eral circulation of the lower stratosphere and troposphere, *Journal of the atmospheric*
622 *sciences*, *44*(14), 1775–1800.
- 623 McLandress, C., and J. Scinocca (2005), The GCM response to current parameterizations
624 of nonorographic gravity wave drag, *Journal of the atmospheric sciences*, *62*(7), 2394–
625 2413.
- 626 McLandress, C., M. J. Alexander, and D. L. Wu (2000), Microwave Limb Sounder obser-
627 vations of gravity waves in the stratosphere: A climatology and interpretation, *Journal*
628 *of Geophysical Research*, *105*(D9), 11,947, doi:10.1029/2000JD900097.
- 629 Nordeng, T. E. (1994), Extended versions of the convective parameterization scheme at
630 ECMWF and their impact on the mean and transient activity of the model in the
631 tropics, *Technical Memorandum 206*, ECMWF, Reading, UK
- 632 Ortland, D. a., and M. J. Alexander (2006), Gravity wave influence on the global structure
633 of the diurnal tide in the mesosphere and lower thermosphere, *Journal of Geophysical*
634 *Research*, *111*(A10S10), 1–15, doi:10.1029/2005JA011467.
- 635 Ortland, D. a., M. J. Alexander, and A. W. Grimsdell (2011), On the Wave Spectrum
636 Generated by Tropical Heating, *Journal of the Atmospheric Sciences*, *68*(9), 2042–2060,
637 doi:10.1175/2011JAS3718.1.

- 638 Pfister, L., S. Scott, M. Lowenstein, S. Bowen, and M. Legg (1993), Mesoscale Distur-
639 bances in the Tropical Stratosphere Excite by Convection: Observations and Effects
640 on the Stratospheric Momentum Budget, *Journal of the atmospheric sciences*, *50*(8),
641 1058–1075.
- 642 Piani, C., and D. Durran (2001), A numerical study of stratospheric gravity waves trig-
643 gered by squall lines observed during the TOGA COARE and COPT-81 experiments,
644 *Journal of the atmospheric sciences*, *58*(1997), 3702–3723.
- 645 Piani, C., D. Durran, M. J. Alexander, and J. R. Holton (2000), A Numerical Study of
646 Three-Dimensional Gravity Waves Triggered by Deep Tropical Convection and Their
647 Role in the Dynamics of the QBO, *Journal of the Atmospheric Sciences*, *57*(22), 3689–
648 3702, doi:10.1175/1520-0469(2000)057<3689:ANSOTD>2.0.CO;2.
- 649 Richter, J. H., F. Sassi, and R. R. Garcia (2010), Toward a Physically Based Gravity Wave
650 Source Parameterization in a General Circulation Model, *Journal of the Atmospheric*
651 *Sciences*, *67*(1), 136–156, doi:10.1175/2009JAS3112.1.
- 652 Ryu, J.-H., M. J. Alexander, and D. a. Ortland (2011), Equatorial Waves in the Up-
653 per Troposphere and Lower Stratosphere Forced by Latent Heating Estimated from
654 TRMM Rain Rates, *Journal of the Atmospheric Sciences*, *68*(10), 2321–2342, doi:
655 10.1175/2011JAS3647.1.
- 656 Salby, M., and R. Garcia (1987), Transient response to localized episodic heating in the
657 tropics. Part I: Excitation and short-time near-field behavior, *Journal of the atmospheric*
658 *sciences*, *44*(2), 458–498.
- 659 Sato, K., and T. Dunkerton (1997), Estimates of momentum flux associated with equato-
660 rial Kelvin and gravity waves, *Journal of geophysical research*, *102*(D22), 26,247–26,261.

- 661 Scaife, A., N. Butchart, C. D. Warner, D. Stainforth, W. Norton, and J. Austin (2000),
662 Realistic quasi biennial oscillations in a simulation of the global climate, *Geophysical*
663 *Research Letters*, *27*(21), 3481–3484.
- 664 Schmidt, H., S. Rast, F. Bunzel, M. Esch, M. Giorgetta, S. Kinne, T. Krismer,
665 G. Stenchikov, C. Timmreck, L. Tomassini, and M. Walz (2013), Response of the mid-
666 dle atmosphere to anthropogenic and natural forcings in the CMIP5 simulations with
667 the Max Planck Institute Earth system model, *Journal of Advances in Modeling Earth*
668 *Systems*, *5*(1), 98–116, doi:10.1002/jame.20014.
- 669 Shibata, K., and M. Deushi (2005), Partitioning between resolved wave forcing and
670 unresolved gravity wave forcing to the quasi-biennial oscillation as revealed with a
671 coupled chemistry-climate model, *Geophysical Research Letters*, *32*(12), L12,820, doi:
672 10.1029/2005GL022885.
- 673 Song, I., H. Chun, and T. Lane (2003), Generation mechanisms of convectively forced
674 internal gravity waves and their propagation to the stratosphere, *Journal of the atmo-*
675 *spheric sciences*, *60*, 1960–1980.
- 676 Stevens, B., M. Giorgetta, M. Esch, T. Mauritsen, T. Crueger, S. Rast, M. Salz-
677 mann, H. Schmidt, J. Bader, K. Block, R. Brokopf, I. Fast, S. Kinne, L. Kornblueh,
678 U. Lohmann, R. Pincus, T. Reichler, and E. Roeckner (2013), Atmospheric component
679 of the MPIM Earth System Model: ECHAM6, *Journal of Advances in Modeling Earth*
680 *Systems*, *5*, 1–27, doi:10.1002/jame.20015.
- 681 Taguchi, M. (2010), Observed connection of the stratospheric quasi-biennial oscillation
682 with El NiñoSouthern Oscillation in radiosonde data, *Journal of Geophysical Research*,
683 *115*(D18), 1–12, doi:10.1029/2010JD014325.

- 684 Tiedtke, M. (1989), A comprehensive mass flux scheme for cumulus parameterization in
685 large- scale models, *Monthly Weather Review*, *117*(8), 1779–1800.
- 686 Wallace, J., R. Panetta, and J. Estberg (1993), Representation of the equatorial strato-
687 spheric quasi-biennial oscillation in EOF phase space, *Journal of the atmospheric sci-*
688 *ences*, *50*(12), 1751–1762.

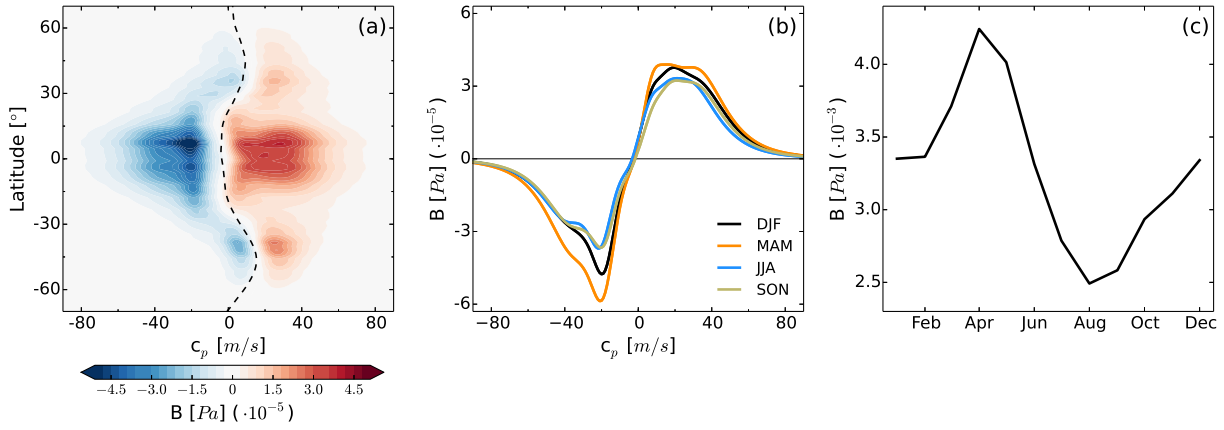


Figure 1. Source spectrum B of zonal momentum flux and its seasonal variability. (a) Latitudinal distribution of time and zonal mean source momentum flux as a function of phase speed. The dashed black line shows the zonal mean wind at 700hPa, the basis for the Doppler shift of the spectrum. (b) Zonal and meridional (5°N to 5°S lat) mean source spectra of zonal momentum flux in the four seasons. (c) Annual cycle of total zonal momentum flux B , zonal and meridional (5°N to 5°S lat) mean integrated over phase speed. All time averages cover 30 years (a-c).

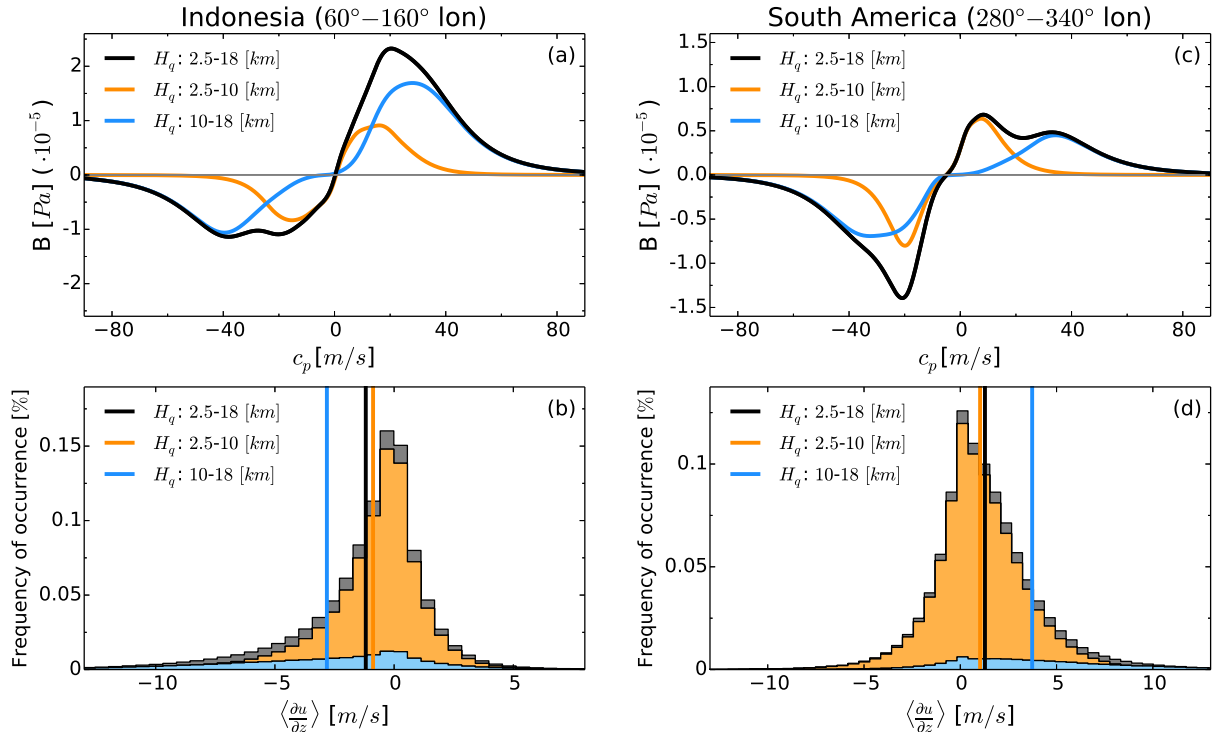


Figure 2. Effect of the background wind on the source spectrum, shown for two selected regions, centered over Indonesia (60° - 160° lon) (a,b) and over South America (280° - 340° lon) (c,d). Colours illustrate different regimes of heating depth: contribution from shallow heating depths (2.5 - 10 km, orange) and from large heating depths (10 - 18 km, blue) to the entire range (2.5 - 18 km, black). Zonal, meridional (5° N to 5° S lat) and time (5 years) mean source spectra of zonal momentum flux (a,c). The spectral asymmetry is caused by wind shear $\langle \frac{\partial U}{\partial z} \rangle$, relative to the zonal wind at $700hPa$, within the vertical extent of the heating. The histogram of wind shear $\langle \frac{\partial u}{\partial z} \rangle$ is shown for different regimes of cloud heating depths (b,d) while the vertical lines denote the distribution mean.

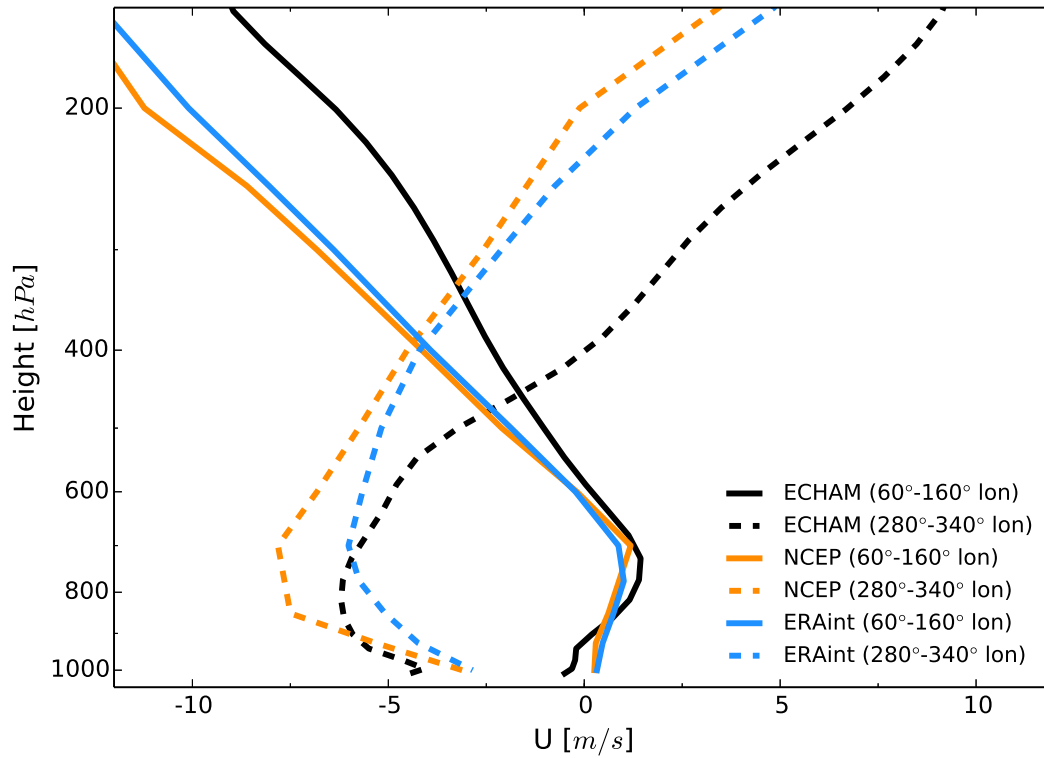


Figure 3. Zonal, meridional (5°N to 5°S lat) and time mean vertical wind profile for two regions, covering the eastern Indian ocean and Indonesia ($60^{\circ} - 160^{\circ}$ lon, solid) and South america ($280^{\circ} - 340^{\circ}$ lon, dashed). Comparison of ECHAM6-Beres simulation (black) with two reanalysis products: NCEP (orange) and ERA-Interim (blue). ECHAM6-Beres covers 30 years, NCEP 62 years and ERA-Interim 20 years.

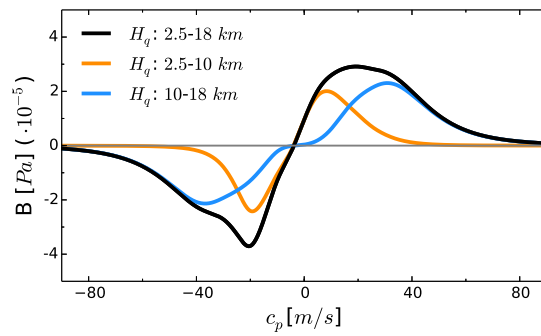


Figure 4. Separation of source spectrum into regimes of heating depth H_q . Zonal, meridional (5°N to 5°S lat) and time (5 years) mean source spectrum B for all cloud heating depths (black), shallow cloud heating depths (orange) and deep cloud heating depths (blue).

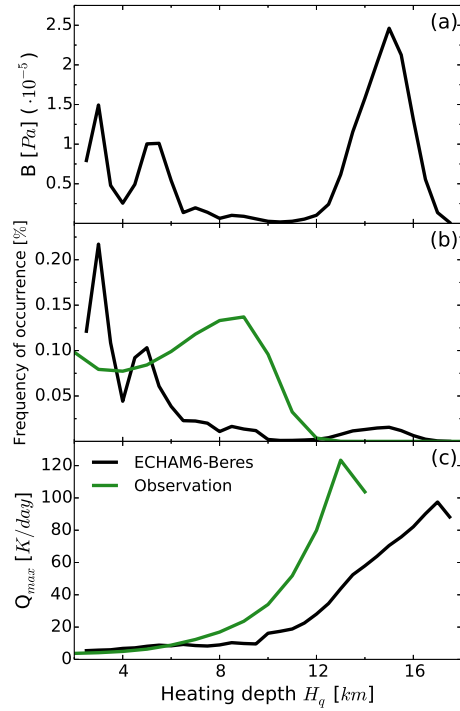


Figure 5. Influence of convection properties on the source momentum flux B (a) as a function of heating depth. Heating depth distribution (b) and maximum heating rate within a GCM grid box (c) (black) are compared to estimated observations (green) derived from geostationary infrared satellite data and TRMM.

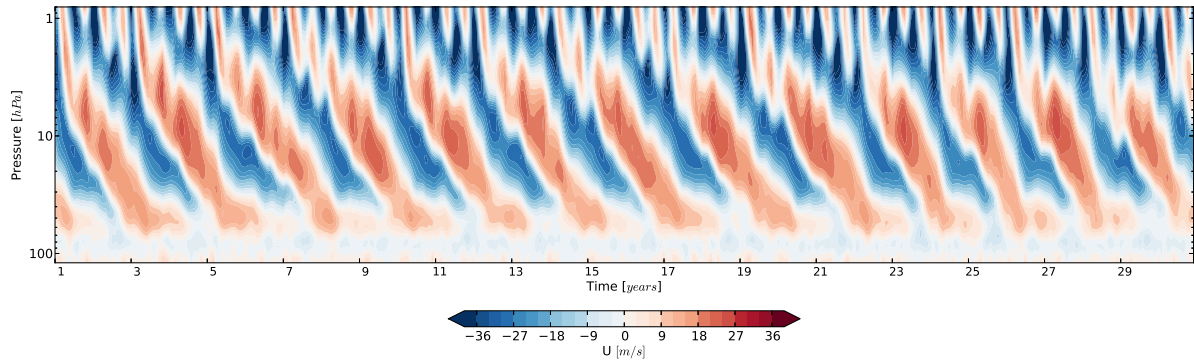


Figure 6. The QBO. Timeseries of meridional (5°N to 5°S lat) and zonal mean zonal wind from a 30year model run with a purely convection based gravity wave source parameterization.

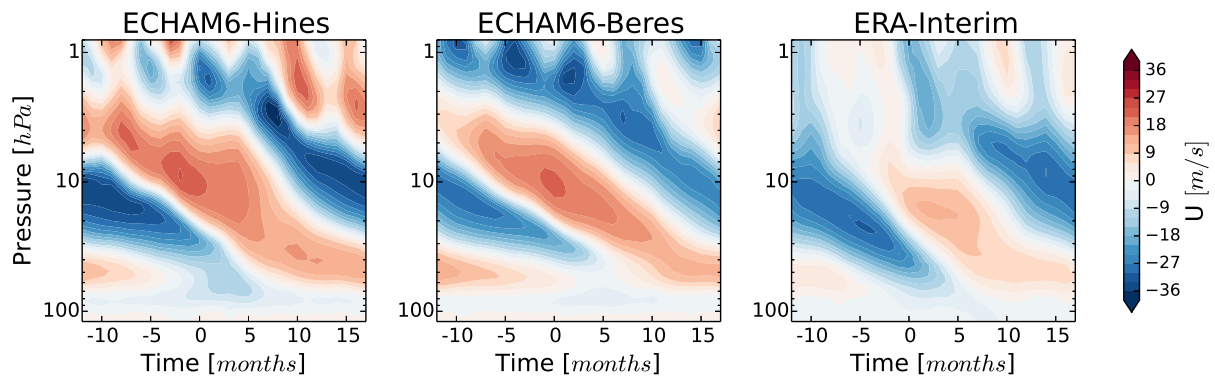


Figure 7. QBO composites of meridional (5°N to 5°S lat) and zonal mean zonal wind. Criterion for the composite is the onset of the westerly jet at $20hPa$. Comparison of the GW parameterization with constant sources (ECHAM6-Hines) with the convection based GW parameterization (ECHAM6-Beres) and reanalysis (ERA-Interim).

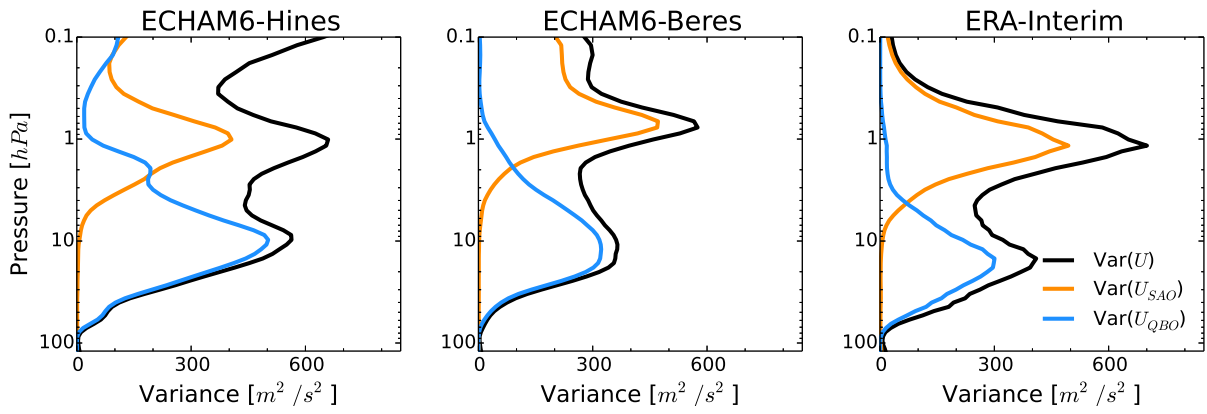


Figure 8. Variance over time (30 years) of meridional (5°N to 5°S lat) and zonal mean zonal wind. In order to compute $\text{Var}(U_{SAO})$ in orange and $\text{Var}(U_{QBO})$ in blue, a Fourier transform in time is applied to the winds, the periods between 5 and 7 months (SAO) and between 23 and 35 months (QBO) are selected to calculate each variance contribution. The variance over all periods $\text{Var}(U)$ is depicted in black. Comparison of the GW parameterization with constant sources (ECHAM6-Hines) with the convection based GW parameterization (ECHAM6-Beres) and reanalysis (ERA-Interim).

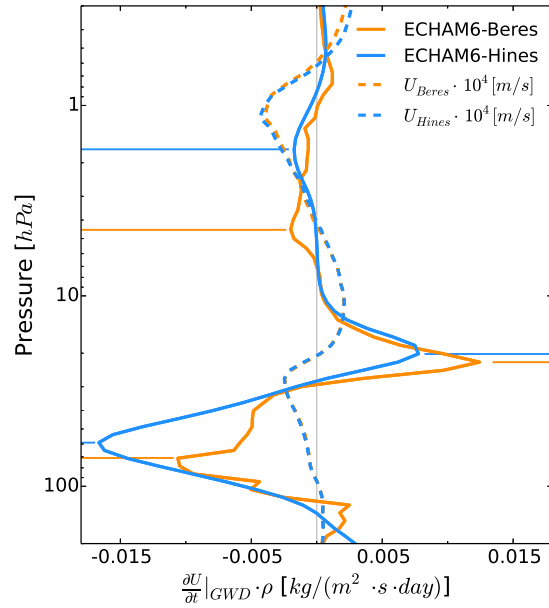


Figure 9. Comparison of GW drag ($\frac{\partial U}{\partial t}|_{GWD}$) profiles of ECHAM6-Beres (orange) with ECHAM6-Hines (blue), drag is scaled by density. Maxima in the drag profiles are emphasized by horizontal lines in according colours, wind profiles are dashed. Zonal and meridional (5°N to 5°S lat) mean over one month.

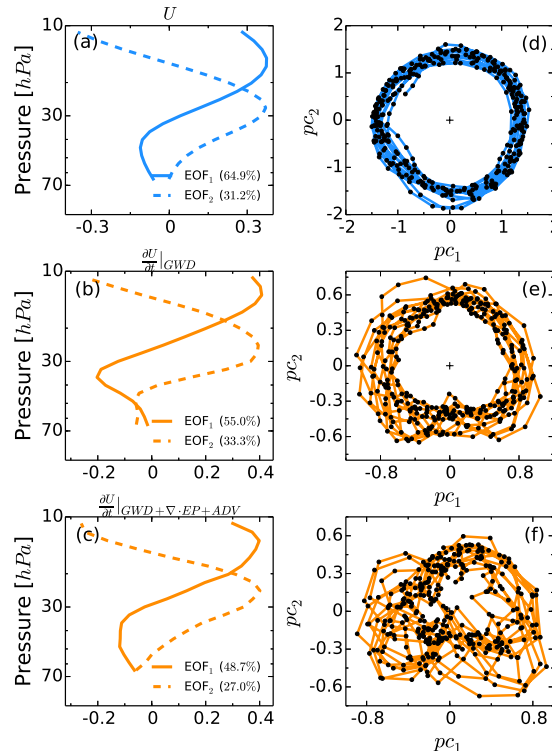


Figure 10. Empirical orthogonal functions (*EOF*) (a)-(c) and principal components (*pc*) (d)-(f) of zonal wind U (a,d), GW drag $\frac{\partial U}{\partial t}|_{GWD}$ (b,e) and the sum of all drag components $\frac{\partial U}{\partial t}|_{GWD+\nabla\cdot EP+ADV}$ (c,f). The numbers in the legend (a)-(c) indicate the fraction of variance that each *EOF* accounts for. The *pcs* in (d) are scaled to unit variance, units on individual plots are arbitrary. The *EOFs* and *pcs* of $\frac{\partial U}{\partial t}|_{\nabla\cdot EP}$ and $\frac{\partial U}{\partial t}|_{ADV}$ are not shown individually; they are qualitatively similar to $\frac{\partial U}{\partial t}|_{GWC}$ in (b,e).

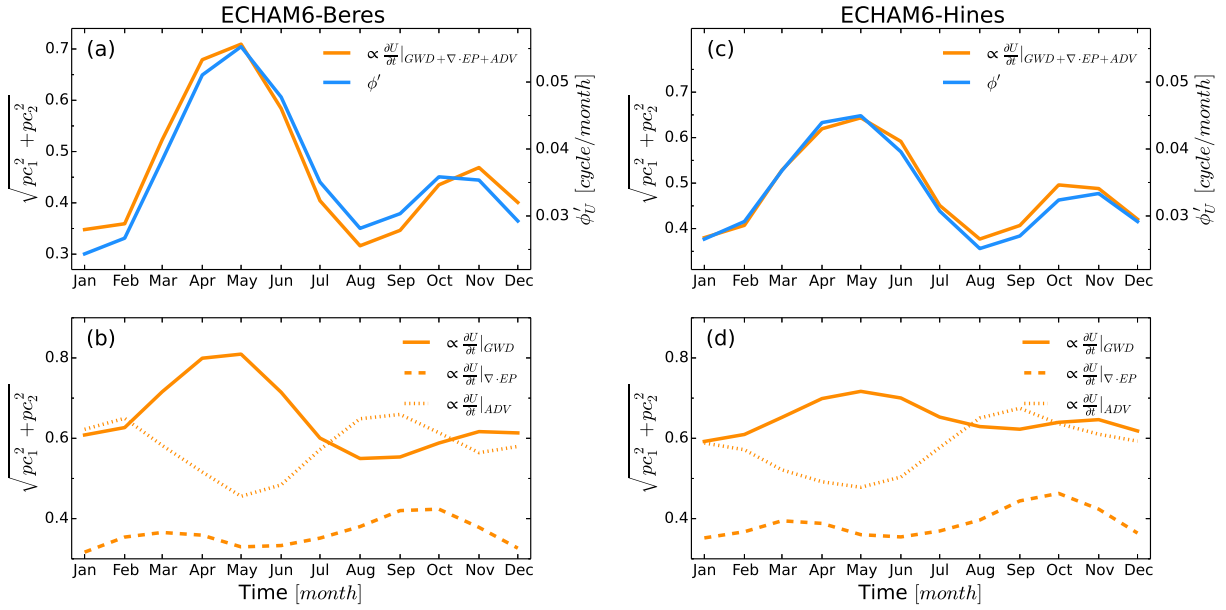


Figure 11. Seasonal cycle of progression of qbo phases (blue) and seasonal cycle of amount of drag (orange) for the Beres (a,b) and the Hines scheme (c,d). Comparison of qbo phase progression (blue) with amount of all drag components (orange) for the Beres (a) and the Hines (c) scheme. Comparison of the individual drag components of the entire drag budget for the Beres (b) and the Hines (d) scheme. The drawn drag is proportional to the actual drag values, units are arbitrary. Note the two different y-axis in (a,c).

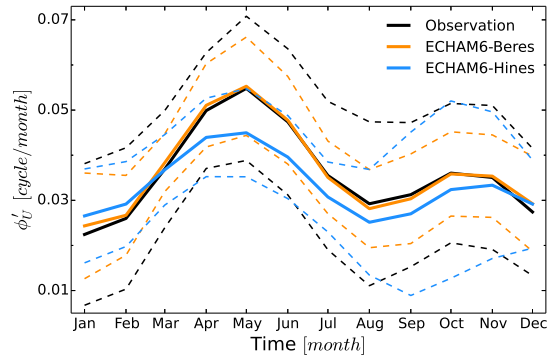


Figure 12. Sesaonal cycle of progression of qbo phases ϕ' . The comparison with radiosonde observations from FU Berlin (black) shows an improvement of the convection based GW parameterization in ECHAM6-Beres (orange) over ECHAM6-Hines with a GW parameterization with constant sources (blue). Dashed lines show the $2\text{-}\sigma$ range.